Formation of black hole stars via star–black hole collisions

Yanlong Shi [1], Qingru Hu [2], Zhenghao Xu [3,2], Douglas N. C. Lin [4,5,6] and Norman Murray [1]

[1] Canadian Institute for Theoretical Astrophysics, University of Toronto, Toronto, ON M5S 3H8, Canada
[2] Department of Astronomy, Tsinghua University, Beijing, 100084, China
[3] Department of Physics, University of California, Santa Barbara, CA 93106, USA
[4] Department of Astronomy, Westlake University, Hangzhou, Zhejiang, 310030, China
[5] Department of Astronomy and Astrophysics, University of California, Santa Cruz, CA, 95064, USA
[6] Institute for Advanced Study, Tsinghua University, Beijing, 100084, China

ABSTRACT

In dense stellar environments such as globular clusters and active galactic nucleus (AGN) disks, stellar-mass black holes (sBHs) may frequently collide with massive stars. We investigate this process using semi-analytic models, three-dimensional hydrodynamical simulations, and one-dimensional stellar evolution calculations, focusing on collisions between sBHs and a $100\,M_\odot$ main-sequence star. We find that gas drag retains the BH within the stellar envelope unless the impact velocity exceeds $\sim 2\sqrt{G(M_\star + M_\bullet)/R_\star}$. The post-collision outcome depends primarily on the BH-to-star mass ratio. For $M_\bullet \gtrsim 30\,M_\odot$, the retained envelope is either quasi-spherical or disc-like, but remains dynamically unstable because of shock heating. In contrast, for $M_\bullet \lesssim 10\,M_\odot$, the collision forms a "black hole star" (BH*): a quasi-hydrostatic, extended stellar envelope surrounding the embedded BH. These results agree with our analytic prediction that BH* formation necessarily requires $M_\bullet \lesssim 0.2\,M_\star$. Follow-up `MESA` calculations further show that, for these low-mass BHs, the shock-heated remnant thermally relaxes without triggering runaway expansion. We discuss several astrophysical implications of BH*s, including their evolution, the possibility of gravitational-wave events from BH binaries assembled within a stellar envelope, and repeated star–sBH collisions as a pathway for rapid BH growth in dense stellar systems. This mechanism may contribute to the formation of massive BHs in high-redshift nuclear star clusters and may be relevant to the origin of the "little red dots" discovered by JWST.

Keywords: Stellar mass black holes (1611), Stellar evolution (1599), Young star clusters (1833), Active galactic nuclei (16), Gravitational wave sources (677)

1. INTRODUCTION

The recent discovery by JWST of a population of compact, red sources at high redshift ($z \gtrsim 4$), dubbed "little red dots" (LRDs, e.g., Matthee et al. 2024; Kokorev et al. 2024; Kocevski et al. 2025), has raised fundamental questions about the evolution of black holes (BHs) in the early Universe. Apart from their compact morphology, LRDs exhibit unique spectral features, like a blue rest-frame UV continuum declining with frequency, a red optical slope with a prominent Balmer break, and broad hydrogen emission lines indicative of gas velocities $\sim 1000\,\mathrm{km\,s^{-1}}$. Among many possible scenarios of LRDs (Inayoshi & Ho 2025), one compelling resolution is the "black hole star" (or "quasi-star," we abbreviate it as "BH*" thereafter) interpretation (e.g., de Graaff et al. 2025a; Begelman & Dexter 2026; Inayoshi et al. 2026; Sun et al. 2026; Naidu et al. 2026): an intermediate-mass/supermassive black hole (IMBH/SMBH) embedded in a massive gaseous envelope simultaneously produces some of the key features: e.g., the gaseous envelope sets $T_{\rm eff} \sim 5000\,\mathrm{K}$ blackbody radiation and reproduces the observed red continuum (e.g., Begelman & Dexter 2026; Inayoshi et al. 2026; de Graaff et al. 2025a); the extended stellar atmosphere gives rise to the Balmer break through hydrogen bound-free absorption (Inayoshi & Maiolino 2025; Naidu et al. 2025; de Graaff et al. 2025b; Sun et al. 2026); the virial motion and electron scattering outside the envelope explain the

Corresponding author: Yanlong Shi
yanlong@cita.utoronto.ca

broad emission lines (Inayoshi et al. 2026; Kokorev et al. 2026).

BH*s are not merely an ad hoc solution to the LRD puzzle, since the theoretical possibility of compact objects embedded in stellar envelopes has a long history. The concept was pioneered by Thorne & Zytkow (1977), who showed that a neutron star engulfed by a giant stellar envelope can reach a quasi-hydrostatic equilibrium, forming a Thorne–Żytkow object (TŻO; Thorne & Zytkow 1977; Hirai & Podsiadlowski 2022). TŻOs produce distinctive nucleosynthetic signatures that have been tentatively identified in observations (e.g., Levesque et al. 2014). BH*s are the natural higher-mass analogue: rather than a neutron star, a BH sits at the center of the envelope, with its accretion luminosity providing additional pressure support in place of nuclear shell burning (e.g., Begelman et al. 2008; Volonteri & Begelman 2010; Ball et al. 2011; Coughlin & Begelman 2024; Hassan et al. 2026).

A natural formation channel for BH*s is the direct collision between a stellar-mass BH (sBH) and a massive star (e.g., Rantala 2026). Such collisions are expected to be frequent in two broad classes of dense stellar environment: nuclear star clusters and globular clusters, where high stellar densities and velocity dispersions drive repeated dynamical encounters (Binney & Tremaine 2008; Rantala 2026), and AGN disks, where the gas-rich environment traps stars and compact objects in a common plane and further enhances collision rates (e.g., Tagawa et al. 2020; Yang et al. 2022; Chen & Lin 2024). Depending on the BH mass, impact parameter, and relative velocity, a star–sBH collision can result in one of several outcomes (refer discussions in Rantala 2026). (1) When both objects closely interact but not yet geometrically collide, the star may undergo a "micro tidal disruption event" (micro-TDE; e.g., Perets et al. 2016; Kremer et al. 2019; Ryu et al. 2022; Vynatheya et al. 2024; Xin et al. 2024; Kıroğlu et al. 2025; Rastello et al. 2026) in the most violent limit. (2) When the BH and the star geometrically collide, a more violent disruption of the star may happen (e.g., Kremer et al. 2022; Hirai & Podsiadlowski 2022; Tsuna & Lu 2025); repeated star–sBH collisions may boost the formation of IMBHs (Rose et al. 2022). (3) On the other hand, in less energetic collisions (the released energy is insufficient to disrupt the star), gas drag may decelerate the BH sufficiently for it to be retained within the stellar envelope, forming a BH*—which we focus on in this paper.

The gas drag that governs BH retention is physically related to the drag force studied extensively in the context of common-envelope (CE) evolution (e.g., Ivanova et al. 2013), in which a BH companion spirals inward through the envelope of a giant star. In CE studies, the drag is typically modeled in the Bondi–Hoyle–Lyttleton (BHL; Hoyle & Lyttleton 1939; Bondi 1952; Edgar 2004) framework or via the energy formalism, which sets the inspiral timescale and envelope ejection (e.g., Ricker & Taam 2012; MacLeod & Ramirez-Ruiz 2015a; Cruz-Osorio & Rezzolla 2020). The star–sBH collision problem shares this drag physics but operates in a qualitatively different regime, since the BH enters the star impulsively at high velocity, depositing energy through a strong shock on dynamical timescales.

Prior simulation works have studied star–sBH collisions primarily in the tidal disruption and electromagnetic transient regime (e.g., Kremer et al. 2022; Vynatheya et al. 2024; Xin et al. 2024), while the conditions for BH retention and the resulting post-collision structure have not been systematically explored. In this paper, we address these questions through a combined semi-analytic and hydrodynamical study of collisions between sBHs of mass 5–100 $M_\odot$ and a 100 $M_\odot$ main-sequence star, a representative mass for massive stars in both AGN disks and nuclear star clusters, where runaway stellar mergers preferentially build up the most massive objects (e.g., Portegies Zwart & McMillan 2002; Kremer et al. 2020; Shi et al. 2021; Rantala et al. 2024). Our semi-analytic approach integrates the BH equation of motion under BHL drag, enabling an efficient survey of the full parameter space of BH mass, impact parameter, and initial velocity. We complement this with three-dimensional hydrodynamical simulations using the `GIZMO` code (Hopkins 2015), which resolve the BH dynamics, shock structure, and envelope morphology for a representative subset of cases.

The remainder of this paper is organized as follows. Section 2 presents the semi-analytic model and stellar evolution calculations, focusing on the orbital dynamics and energy budget of the collision. Section 3 describes the hydrodynamical simulations. Section 4 discusses the astrophysical implications of such star–sBH collisions. Section 5 summarizes our findings and future directions.

2. ANALYTICAL EXPECTATIONS

2.1. *The gas dynamical friction*

As an sBH moves through the gas envelope of a massive star, it gravitationally focuses the gas flow into an overdense wake behind it. The weak exerts a gravitational drag on the moving sBH, known as dynamical friction (Chandrasekhar 1943; Ostriker 1999). In the highly supersonic regime, where gas pressure is negligible, Hoyle & Lyttleton (1939) estimated the cross section of this gravitational focusing with the Hoyle–Lyttleton (HL) radius $R_{\rm HL} = 2GM_\bullet/v^2$, where $M_\bullet$ is

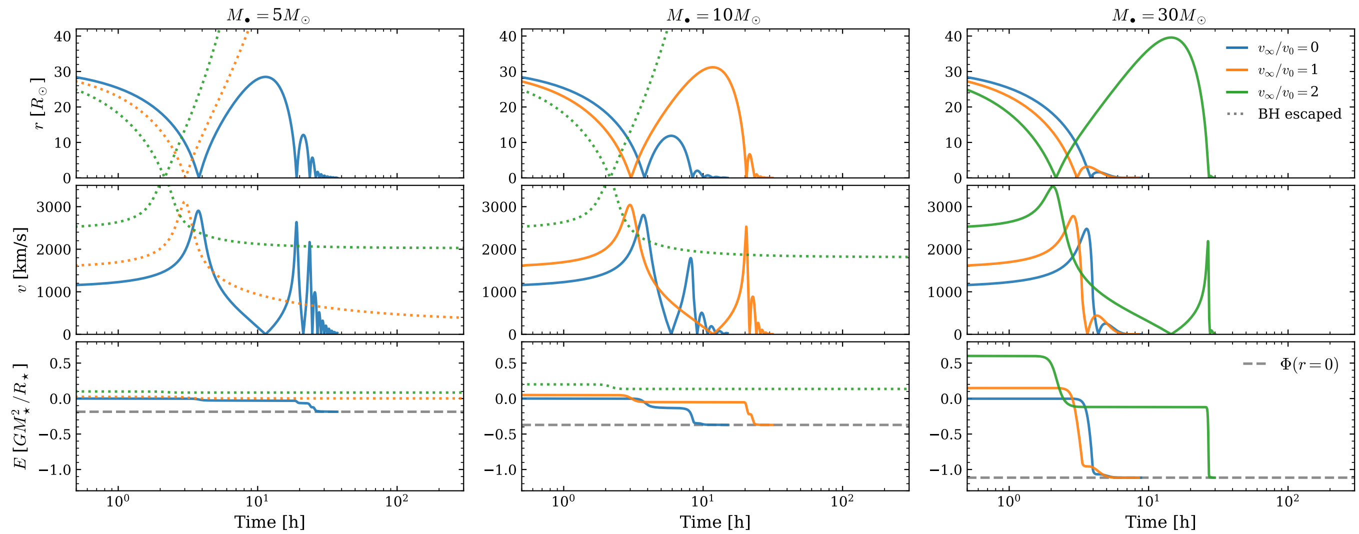

Figure 1. Position (*top panels*), velocity (*middle panels*) and energy (*bottom panels*) evolution for head-on ($b = 0$) star–sBH collisions. Blue, orange, and green lines correspond to $v_\infty/v_0 = 0$, 1, and 2, respectively. Dotted lines indicate semi-analytic simulations where the sBH escapes the star. The gray dashed line in the bottom panel marks the minimum potential at the stellar center $\Phi(r = 0)$.

the sBH mass and v its speed relative to the gas, yielding a drag force $F_{\rm HL} \sim \pi R_{\rm HL}^2 \rho v^2 = 4\pi G^2 M_\bullet^2 \rho / v^2$, with ρ the gas density at the sBH location. While this estimate diverges as $v \to 0$, at mild Mach numbers, the work of Bondi (1952) leads to the interpolation formula

$$F_{\rm drag} \sim \frac{4\pi G^2 M_\bullet^2 \rho\, v}{(c_{\rm s}^2 + v^2)^{3/2}}, \tag{1}$$

where $c_{\rm s}$ is the gas sound speed, recovering $F_{\rm HL}$ when $v \gg c_{\rm s}$ (Edgar 2004). This estimate of the drag forces sets the baseline for a series of succeeding works of linear perturbation analysis (Ostriker 1999) and numerical simulations (e.g., Lescaudron et al. 2023; Suzuguchi et al. 2024), as also reviewed by Röpke & De Marco (2023).

The drag force dissipates the sBH's orbital energy at a rate $\dot{E}_{\rm drag} \sim F_{\rm drag} v$, also referred to as the dynamical friction luminosity, so the sBH kinetic energy is damped on a timescale of

$$\tau_{\rm damp} \sim \frac{M_\bullet v^2/2}{\dot{E}_{\rm drag}} = \frac{(c_{\rm s}^2 + v^2)^{3/2}}{8\pi G^2 \rho M_\bullet}. \tag{2}$$

For typical conditions inside a massive star, e.g., $\rho = 0.2\,{\rm g\,cm^{-3}}$ and $c_{\rm s} = 500\,{\rm km\,s^{-1}}$, an sBH with $M_\bullet = 5\,M_\odot$ moving transonically ($v \approx c_{\rm s}$) is stopped within $\tau_{\rm damp} \approx 0.5\,{\rm h}$, comparable to or shorter than the stellar dynamical time. Such efficient dissipation implies that gas dynamical friction alone may fully damp the orbital energy of an sBH colliding with a massive star, retaining it inside the star. In the following part, we explicitly calculate the orbits of the sBH colliding with a massive star to further quantify this process.

2.2. *Semi-analytic orbital integration*

2.2.1. *Model setups and initial condition*

We consider the simplified limit $M_\bullet \ll M_\star$, in which the massive star can be treated as a fixed background gas cloud when integrating the orbital trajectory of the sBH. This semi-analytic approach is similar to that utilized in CE studies (e.g., MacLeod & Ramirez-Ruiz 2015a,b). The sBH then evolves under the gravity of the background star and the gaseous drag force,

$$\ddot{\boldsymbol{r}} = -\frac{GM_\star(<r)}{r^3}\boldsymbol{r} + \frac{\boldsymbol{F}_{\rm drag}}{M_\bullet}, \tag{3}$$

where $\boldsymbol{r}$ is the sBH position relative to the stellar center and $M_\star(<r)$ is the enclosed stellar mass within radius r. Following Ostriker (1999), the drag force is

$$\boldsymbol{F}_{\rm drag} = -\frac{4\pi G^2 M_\bullet^2 \rho}{v^3}\, I(\mathcal{M})\, \boldsymbol{v}, \tag{4}$$

where $\boldsymbol{v}$ is the sBH velocity, and the prefactor $I(\mathcal{M})$ encodes the dependence on the Mach number $\mathcal{M} \equiv v/c_{\rm s}$. Since the original $I(\mathcal{M})$ of Ostriker (1999) is singular at $\mathcal{M} = 1$, we adopt the regularized form of Generozov & Perets (2023),

$$I(\mathcal{M}) = \begin{cases} \ln\Lambda, & \mathcal{M} \geq 1; \\ \min\left[\ln\Lambda,\ \dfrac{1}{2}\ln\left(\dfrac{1+\mathcal{M}}{1-\mathcal{M}}\right) - \mathcal{M}\right], & \mathcal{M} < 1, \end{cases} \tag{5}$$

where the Coulomb logarithm is set to $\ln\Lambda = 1.4 \sim \ln(R_\star/R_{\rm HL})$, the ratio of the largest to the smallest radial scales contributing to the drag.

We integrate Equation (3) for the sBH orbit using the REBOUNDx package (Tamayo et al. 2020), an extension of the REBOUND code (Rein & Liu 2012), with the 15th-order IAS15 integrator (Rein & Spiegel 2015). The integration terminates when either (1) the distance between the sBH and the stellar center falls below $10^{-3}\,R_\odot$, indicating that the sBH has settled at the stellar center, or (2) the integration time reaches 10^3 hours. We mark the time when the simulation terminates as the "stopping time" $t_{\rm stop}$.

We model the massive star as an $n = 2.75$ polytrope (close to $n = 3$ yet stable), corresponding to $\gamma = 1 + 1/n = 15/11 \approx 4/3$ and an equation of state (EOS) $p = (4/11)\rho e \approx (1/3)\rho e$, where e is the specific internal energy. The star has $M_\star = 100\,M_\odot$ and $R_\star \approx 16\,R_\odot$ (from the main-sequence relation $R_\star = (M_\star/M_\odot)^{0.6}\,R_\odot$; Tout et al. 1996).

The sBH has $M_\bullet \in [5, 30]\,M_\odot$, and is placed at an initial separation $r_0 = 2R_\star$ from the stellar center. For an impact velocity at infinity v_∞, the relative velocity at r_0 is $v = [2G(M_\star + M_\bullet)/r_0 + v_\infty^2]^{1/2} = (v_0^2 + v_\infty^2)^{1/2}$, where $v_0^2 \equiv G(M_\star + M_\bullet)/R_\star$. The velocity direction is set by the impact parameter $b \equiv |\hat{\boldsymbol{v}} \times \boldsymbol{r}_0|$, with $b = 0$ corresponding to a head-on collision. The specific orbital angular momentum is then $l = b\,(v_0^2 + v_\infty^2)^{1/2} = b_\infty v_\infty$, where b_∞ is the impact parameter at infinity. Since $b_\infty \to \infty$ for parabolic orbits ($v_\infty = 0$), we parameterize the initial conditions with b rather than b_∞.

2.2.2. *Critical sBH mass to form a BH**

Figure 1 shows the orbital evolution of sBHs with $M_\bullet = 5$, 10, 30 $M_\odot$ in head-on collisions ($b = 0$) with $v_\infty/v_0 = 0$, 1, 2. From top to bottom, the panels show the position r, the total velocity v, and the total energy $E = M_\bullet(v^2/2+\Phi(r))$ of the sBH, where $\Phi(r)$ is the gravitational potential energy due to the background star,

$$\Phi(r) = \begin{cases} -GM_\star/r, & r \geq R_\star; \\ -GM_\star(<r)/r - G\int_r^{R_\star} 4\pi r'\rho(r')\mathrm{d}r', & r < R_\star. \end{cases} \tag{6}$$

All sBHs that are eventually retained inside the star are stopped within dozens of hours, i.e., a few stellar dynamical times, consistent with the order-of-magnitude estimate in Section 2.1. Most of the energy dissipation occurs near the stellar core, where the higher gas density strengthens the dynamical friction. More massive sBHs are damped faster, as expected from Equation (2): for $v_\infty/v_0 = 0$, the stopping time decreases from ~ 37 h at $M_\bullet = 5\,M_\odot$ to ~ 9 h at $M_\bullet = 30\,M_\odot$. They also deposit more energy: for $M_\bullet = 30\,M_\odot$, the dissipated energy becomes comparable to the stellar binding energy ($\sim GM_\star^2/R_\star$), implying significant envelope expansion and possibly substantial mass loss.

Consequently, there exists a critical sBH mass above which the dissipative heating injects enough energy to disrupt the host star, setting a natural upper limit for an sBH to be retained and form a BH*. Our semi-analytic simulations yield a first-order scaling between this critical mass and the stellar mass. As illustrated by the gray dashed lines in the bottom panels of Figure 1, the final energy of an sBH settling at the stellar center equals its local potential energy, $\Phi(r = 0) = -3.80\,GM_\star/R_\star$, with the numerical coefficient set by the polytropic index $n = 2.75$. For mild velocities at infinity, the energy dissipated into the stellar envelope is $E_{\rm drag} = M_\bullet(v_\infty^2/2 - \Phi(r = 0)) \approx -M_\bullet\Phi(r = 0)$. The binding energy of a polytropic star is $E_{\rm bind} = -\alpha(n)\,GM_\star^2/R_\star$ (Chandrasekhar 1957), where $\alpha(n) = 3/[2(5-n)] \approx 0.67$ for $n = 2.75$. Equating $|E_{\rm drag}|$ with $|E_{\rm bind}|$ yields a maximum sBH mass that scales linearly with the stellar mass,

$$M_{\bullet,\rm max} \approx \frac{0.67\,GM_\star^2/R_\star}{3.80\,GM_\star/R_\star} \approx 0.2\,M_\star. \tag{7}$$

This condition holds for massive star that can be approximated with $n \lesssim 3$. For $M_\star = 100\,M_\odot$, the critical sBH mass is $M_{\bullet,\rm max} \approx 20\,M_\odot$, so more massive sBHs (e.g., $30\,M_\odot$) may drive significant envelope ejection.

2.2.3. *Critical collisional parameters to retain the BH*

Another important question is with what collisional parameters (b, v_∞) can the sBH be retained at the center of the star after a collision. In our example head-on ($b = 0$) collisions in Figure 1, there is an emerging trend more massive sBHs can be easier to be retained despite at a higher velocity (v_∞). To quantatively study this problem, we first fix the impact parameter to $b = 0$, and perform a parameter survey over the sBH mass ($M_\bullet$) and velocity at infinity (v_∞) to determine the retention boundary. The results are presented in the left panel of Figure 2, where gray dots mark the $M_\bullet$–v_∞ parameter space leading to an escape, while the colored mesh indicates the stopping time for retained sBHs. The retention boundary, marked by the red dashed line, generally increases with sBH mass and can be well-fitted by a quadratic polynomial ($v_\infty/v_0 = -0.000949(M_\bullet/M_\odot)^2 + 0.0772(M_\bullet/M_\odot) + 0.594$). For sBHs with $M_\bullet \lesssim 30\,M_\odot$, the maximum velocity at infinity is constrained to $v_\infty \lesssim 2v_0 = 2\sqrt{G(M_\star + M_{\rm bh})/R_\star}$. Inside the retention boundary, sBHs will be damped to the star's center in ~ 10–100 h.

We note that while massive sBHs can be efficiently retained in the star, the collision may not form a BH*

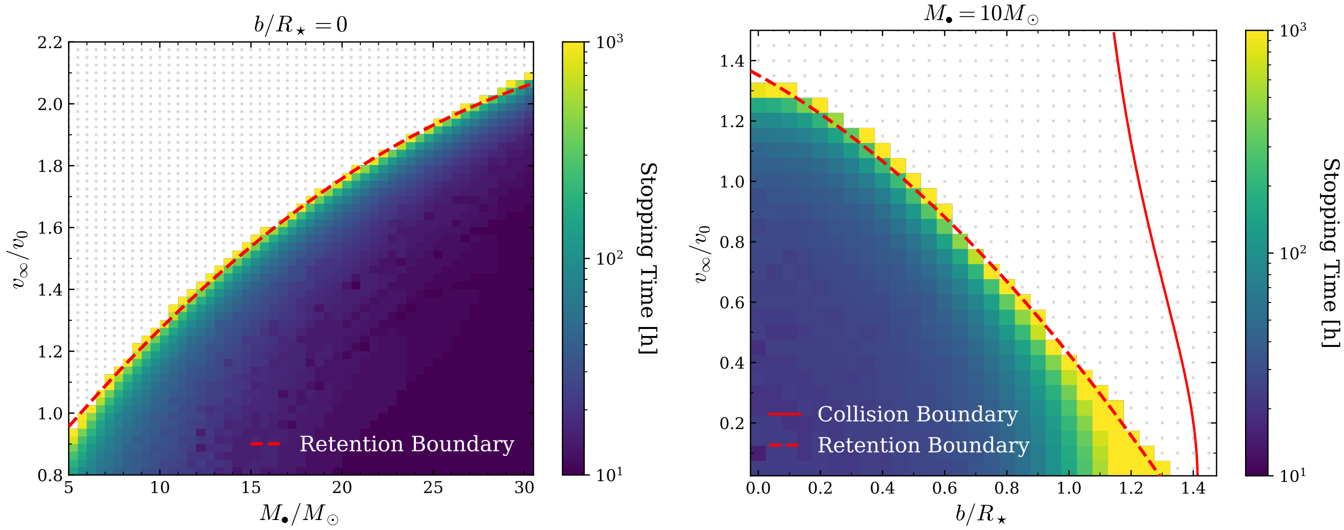

Figure 2. Critical collisional parameters (b, v_∞) for an sBH to be retained in the massive star and form a BH*, which implies a finite stopping time ($t_{\rm stop}$) through our numerical orbital integration (Section 2). *Left*: the stopping time in the parameter space of $(M_\bullet/M_\odot, v_\infty/v_0)$, assuming head-on collisions ($b/R_\star = 0$). The colored mesh plot indicates the stopping time (in hours) for sBHs that successfully remain inside the star. Grey dots represent the parameter space where the sBH fails to be retained by the star. The dashed red line approximates the retention boundary. *Right*: similar to the left panel, but in the parameter space of $(b/R_\star, v_\infty/v_0)$, assuming fixed $M_\bullet = 10\,M_\odot$. The solid red line represents the critical boundary for an sBH to geometrically collide with the star, and the dashed red line outlines the critical boundary for an sBH to be retained within the star.

if the sBH mass is above the threshold ($\sim 0.2\,M_\star$, cf. Equation 7).

Whether the sBH can be captured also depends critically on the impact parameter b. Taking a representative sBH with $M_\bullet = 10\,M_\odot$, we conduct a grid search over b and v_∞ to map the retention threshold. The results are displayed in the right panel of Figure 2, where the red dashed line represents the retention boundary, which is well-fitted with $v_\infty/v_0 = -0.352(b/R_\star)^2 - 0.572(b/R_\star) + 1.35$, and the solid red line marks the geometric collision boundary. At low v_∞, the critical impact parameter for retention is comparable to the geometric collision threshold. However, as v_∞ increases, the critical retention impact parameter deviates rapidly. Ultimately, when $v_\infty \sim 1.4\,v_0$, only head-on ($b = 0$) collisions can marginally retained the sBH inside the star. However, for most sBHs retained in the star, the stopping time is still $\sim$ 10–100 h.

2.3. *Dissipative heating of the star*

While the semi-analytic model in Section 2.2.2 and Section 2.2.3 follows the orbital evolution of the sBH, it does not include the response of the background star to the dissipated orbital energy, which simultaneously heats the stellar interior. This energy injection may cause envelope expansion and mass loss, and additionally, it may raise the temperature of the nuclear-burning zone and boost the burning rate, potentially triggering a thermal runaway if the star cannot adjust quickly enough. To address this concern, we use `MESA` to calculate the one-dimensional stellar response to the dissipative heating of the star by the damping of the sBH orbit (Paxton et al. 2011, 2013, 2015, 2018, 2019; Jermyn et al. 2023). Our setup builds on previous massive AGN-star calculations with `MESA` (Cantiello et al. 2021; Ali-Dib & Lin 2023; Xu 2025; Xu et al. 2026).

We begin with a non-rotating main–sequence stellar model with $M_\star = 100M_\odot$ and $R_\star \approx 16R_\odot$. The orbital energy dissipated by the sBH is added through the `other_energy` hook as an external specific heating term. The total additional energy is given as

$$E_{\rm inj} = f\frac{GM_\star^2}{R_\star}. \tag{8}$$

The time dependence of the additional heating is taken from the calculation in Section 2.2 as well in Figure 1, which records the sBH's position $r(t)$ and the corresponding dissipated $E_{\rm inj}(t)$. We assume the dynamical-friction luminosity is proportional to the energy dissipation and linearly interpolate the curve. We damp the energy to stellar mesh cells between $q_{\rm min}$ and $q_{\rm max}$ where q is the normalized radial distance. At each timestep, the interpolated luminosity is converted to a specific heating rate and is applied to the injected stellar cells between $q_{\rm min}$ and $q_{\rm max}$. With this additional source term, `MESA` continues its calculations of stellar structure and evolution.

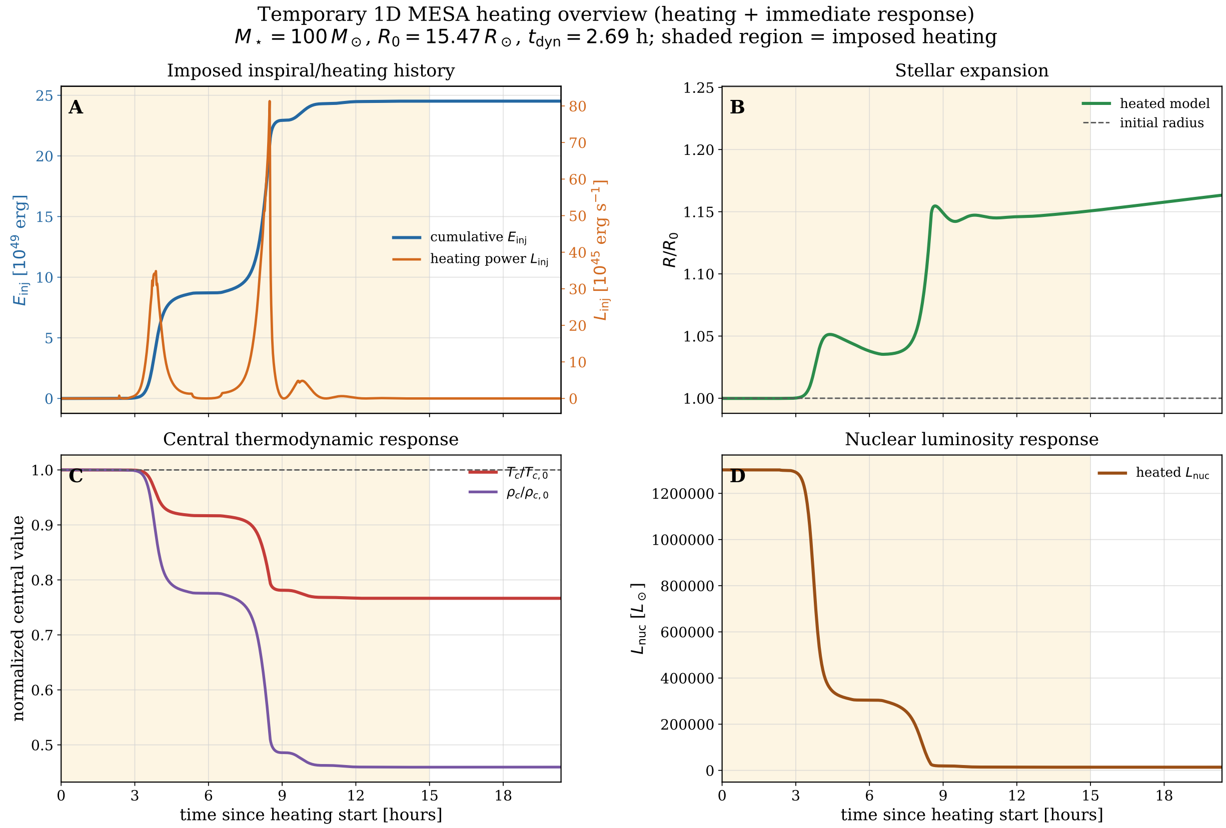

Figure 3. Response of the fiducial $100\,M_\odot$ stellar model to imposed inspiral heating of a $10\,M_\odot$ sBH with $b = 0$ and $v_\infty = 0$. The shaded region marks the heating interval. Panel (a) shows the cumulative injected energy and heating luminosity. Panel (b)—(d) show the stellar expansion in radius, central temperature and density, and nuclear luminosity. The shaded region marks the heating interval.

The evolution followed here is much shorter than the characteristic growth time of the Eddington–limited sBH, so its mass changes negligibly. Moreover, the dynamical friction luminosity is much larger than the Eddington-limited accretion luminosity of the sBH, making accretion feedback energetically subdominant during the inspiral. We evolve the model to $50\,t_{\rm dyn}$ after the onset of heating.

Figure 3 shows the fiducial stellar response. For the fiducial calculation, we use the luminosity history of a $10\,M_\odot$ sBH with $b = 0$ and $v_\infty = 0$. The total injected energy is $0.1\,GM_\star^2/R_\star = 6.79 \times 10^{49}$ erg. The heating lasts $5.39 \times 10^4\,{\rm s} = 14.97\,{\rm h} = 5.6\,t_{\rm dyn}$.

The radius increases from $15.47\,R_\odot$ to $17.95\,R_\odot$ during the heating phase and reaches $19.18\,R_\odot$ by the end of the calculation. The expansion is accompanied by decreases of approximately 15% in T_c and 35% in ρ_c. The nuclear luminosity falls from $1.30 \times 10^6\,L_\odot$ to $1.37 \times 10^4\,L_\odot$ by the end of heating. The model therefore expands and cools without developing a nuclear runaway over the computed interval.

The star's expansion is accompanied by decreases of approximately 15% in $T_{\rm c}$ and 35% in $\rho_{\rm c}$, consistent with the scalings $T_{\rm c} \propto R_\star^{-1}$ and $\rho_{\rm c} \propto R_\star^{-3}$. The nuclear luminosity decreases more strongly because of the steep temperature dependence of CNO burning near $T_{\rm c} \simeq 2 \times 10^7$ K (Paxton et al. 2013, 2015). Thus, the model expands and cools rather than developing a nuclear runaway over the computed interval.

We also vary the injected-energy fraction, expressed relative to the stellar gravitational-energy scale in Equation 8, and the damping time while keeping $M_\star = 100\,M_\odot$ and $0 \le q \le 0.8$ fixed. The completed models cover $f = 0.03$, 0.1, 0.3 or $0.5\,GM_\star^2/R_\star$. The calculations with $f = 0.5$ terminate before the end of the heating phase because of excessive expansion.

These one-dimensional models isolate the thermal response to orbital energy dissipation. The wake, shocks, angular-momentum deposition, and dynamical mass loss are followed in the hydrodynamical simulations in Section 3.

3. HYDRODYNAMICAL SIMULATIONS

The results in Section 2.3 indicate that energy dissipation during the sBH's orbital decay can lead to changes in the massive main-sequence star's interior. However,

Table 1. Parameter space of the hydrodynamical simulations, including the sBH mass ($M_\bullet$), impact parameter (b, defined in Section 2.2.1, which is *not* the impact parameter at infinity), and relative velocity at infinity (v_∞) with the velocity direction set by the impact parameter. Here $v_0^2 \equiv G(M_\star + M_\bullet)/R_\star$. The non-spinning stars are fixed with $M_\star = 100\,M_\odot$ for all simulations, and are modeled with $n = 2.75$ polytopes by default.

$M_\bullet\,[M_\odot]$	$b\,[R_\star \approx 16\,R_\odot]$	v_∞/v_0 ($v_\infty\,[\mathrm{km\,s^{-1}}]$)
5	0, 0.5	0, 1 (1124), 2 (2248)
10	0, 0.5	0, 1 (1151), 2 (2302)
30	0, 0.5	0, 1 (1251), 2 (2502)
100	0, 0.5	0, 1 (1552), 2 (3104)

this 1-D `MESA` model does not fully capture the rapid 3-D dynamical response of the stellar envelope. In this section, we perform a suite of hydrodynamical simulations of star–sBH collisions, using the Lagrangian code `GIZMO` (Hopkins 2015). The simulations solve the standard hydrodynamical equations[1] with the code's Meshless Finite-Mass (MFM) mode, and self-gravity is solved with tree-gravity (Hopkins et al. 2023).

Each initial condition for the simulations includes a massive star and a companion BH (cf. Section 2.2.1). The star is fixed as an $n = 2.75$[2], $100\,M_\odot$ polytrope with 128^3 equal-mass gas cells ($\Delta m \sim 5 \times 10^{-5}\,M_\odot$), which is generated following Ohlmann et al. (2017) and Shi et al. (2026).

3.1. *Simulation setups*

The simulation setups are summarized in Table 1. In each pair of $(M_\star, M_\bullet)$, we set different collisional parameters, via $b/R_\star = 0, 0.5$, and $v_\infty/v_0 = 0, 1, 2$. This covers cases like head-on vs. "grazing" collisions, and parabolic vs. hyperbolic orbits. Each simulation runs for $50\,\tau_{\mathrm{dyn},\star} \approx 140\,\mathrm{h}$ (where $\tau_{\mathrm{dyn},\star} = [R_\star^3/(GM_\star)]^{1/2}$). We label each simulation with `Mbh%g_b%g_v%g`, representing the BH mass ($M_\bullet/M_\odot$), impact parameter ($b/R_\star$), and initial relative velocity at infinity (v_∞/v_0).

For gravity, we use fixed, small ($h_{\mathrm{gas}} = 10^{-4}\,R_\odot$) softening radii for the gas cells, and a larger softening radius ($h_{\mathrm{BH}} = 0.5\,R_\odot$) for the sBH, which is compatible with the spatial resolution. This avoids the noisy, unphysical numerical heating of the gas when the BH softening radius is too small, an issue that appeared in many of our background tests. Moreover, the Bondi radius of a $5\,M_\odot$ sBH embedded in a $c_{\mathrm{s}} \approx 1{,}000\,\mathrm{km\,s^{-1}}$ is $R_{\mathrm{Bondi}} = GM_\bullet/c_{\mathrm{s}}^2 \sim R_\odot$; given our mean spatial resolution of $\Delta r \sim 2R_\star/128 \sim 0.2\,R_\odot$, $h_{\mathrm{gas}} \ll \Delta r < h_{\mathrm{BH}} \lesssim R_{\mathrm{Bondi}}$, suggesting that the Bondi radius is resolved.

Our simulations solve only the coupled hydrodynamics and gravity of the star–BH collision. We neglect BH accretion, feedback, and radiation transfer, since our simulation timescale is short ($\sim 140\,\mathrm{h}$): for Eddington-limited BH accretion, the relevant timescale is the Salpeter time $\tau_{\mathrm{Sal}} = 0.1\sigma_{\mathrm{es}}c/(4\pi G m_{\mathrm{p}}) \approx 45\,\mathrm{Myr}$; the thermal (Kelvin-Helmholtz) timescale for an $100\,M_\odot$ star is $\tau_{\mathrm{KH}} \sim GM_\star^2/(2R_\star L_\star) \sim 10^4\,\mathrm{yr}$ (assuming near-Eddington luminosity). Both the accretion and thermal timescales are substantially longer than our simulation timescale (i.e., $\tau_{\mathrm{dyn},\star} \ll \tau_{\mathrm{KH}} \ll \tau_{\mathrm{Sal}}$). Additionally, Murguia-Berthier et al. (2017) found that accretion disks can hardly form in common envelopes, especially in high-density, low-compressibility regions; strong feedback is therefore uncommon, suggesting feedback can also be unimportant.

3.2. *Outcomes of the collisions*

3.2.1. *Morphology*

Figure 4 visualizes a subset of the star–sBH collisional simulations, where $M_\bullet = 10\,M_\odot$, with varying impact parameters and velocities. Each sub-figure displays the density (*upper panel*) and passive scalar (*lower panel*) distributions at the stellar mid-plane. The passive scalar is a post-processed quantity assigned to each gas cell to track mixing during the collision; specifically, its value at $t = 0$ is defined as $p = (R_\star - r)/R_\star$, where r is the distance from the stellar center and $R_\star$ is the stellar radius. While the p-value of each gas cell is advected without change, the overall passive scalar distribution evolves as a result of mixing.

Figure 4a shows the head-on collision ($b = 0$, $v_\infty = 0$) at characteristic times $t = 3.7\,\mathrm{h}$, the BH enters the star with a relative velocity of $2745\,\mathrm{km\,s^{-1}}$, driving a shock wake. Gas drag then decelerates the BH and reverses its direction of motion; by $t = 9.3\,\mathrm{h}$, the BH is moving in the direction opposite to its initial trajectory. Finally, at the end of the simulation ($t = 140\,\mathrm{h}$), the BH is fully decelerated and co-moves with the stellar envelope. The passive scalar distribution traces the accompanying perturbation of the stellar interior.

Figure 4b shows a grazing collision ($b = 0.5\,R_\star$, $v_\infty = 0$). The non-zero angular momentum causes the BH to orbit the center of the gravitational potential (see green

[1] Specifically: (1) $\partial_t\rho + \nabla\cdot(\rho\boldsymbol{v}) = 0$; (2) $\partial_t(\rho\boldsymbol{v}) + \nabla\cdot(\rho\boldsymbol{v}\boldsymbol{v} + p\mathbf{I}) = \rho\boldsymbol{g}$; (3) $\partial_t\left(\rho e + \rho v^2/2\right) + \nabla\cdot\left[\left(\rho e + \rho v^2/2 + p\right)\boldsymbol{v}\right] = \rho\boldsymbol{g}\cdot\boldsymbol{v}$; (4) $p = (\gamma - 1)\rho e$.

[2] We also test $n = 2$ and find qualitatively similar results.

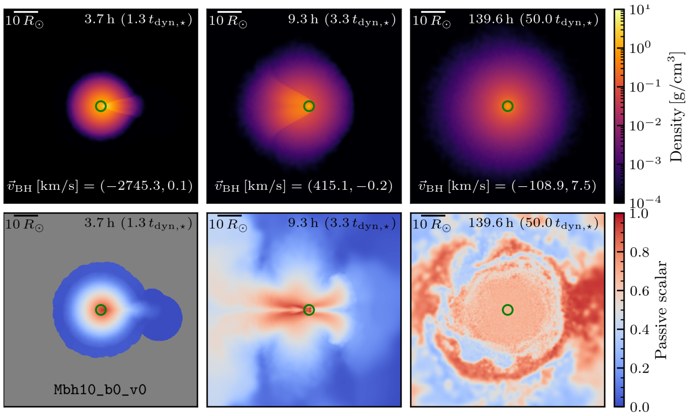

(a) BH mass 10 $M_\odot$. Head-on ($b = 0$) collision with $v_\infty = 0$. Panels in the right column are centered at the sBH's location.

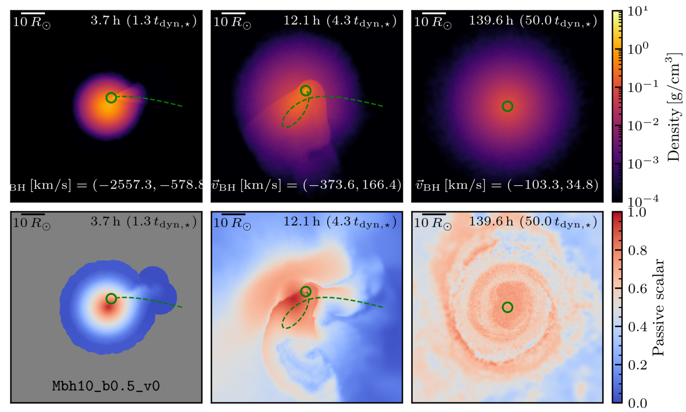

(b) BH mass 10 $M_\odot$. Grazing ($b = 0.5\,R_\star$) collision with $v_\infty = 0$. Panels in the right column are centered at the sBH's location.

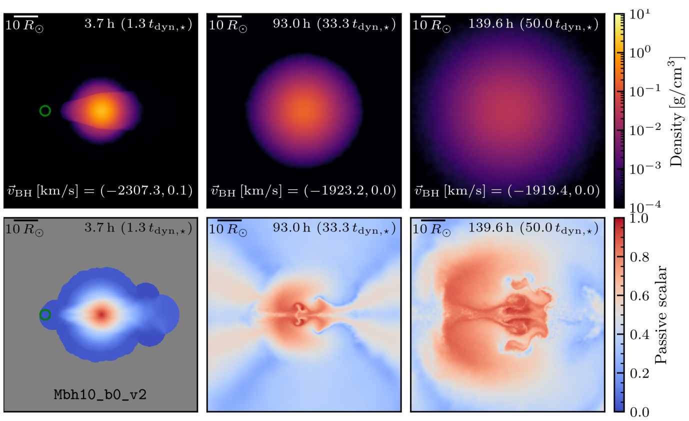

(c) BH mass 10 $M_\odot$. Head-on ($b = 0$) collision with $v_\infty = 2\sqrt{G(M_\star + M_\bullet)/R_\star}$. Panels in the right two columns are centered at the star.

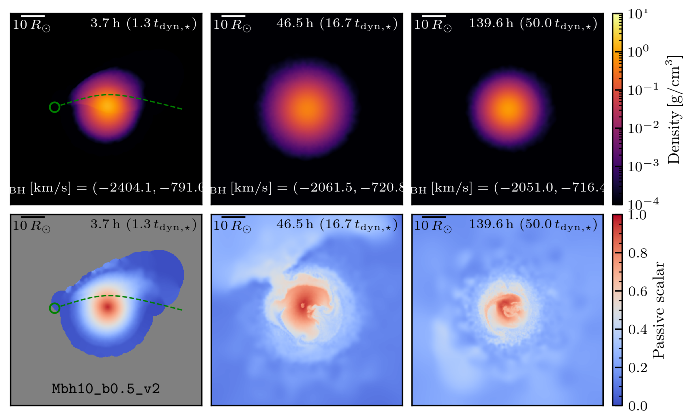

(d) BH mass 10 $M_\odot$. Grazing ($b = 0.5\,R_\star$) collision with $v_\infty = 2\sqrt{G(M_\star + M_\bullet)/R_\star}$. Panels in the right two columns are centered at the star.

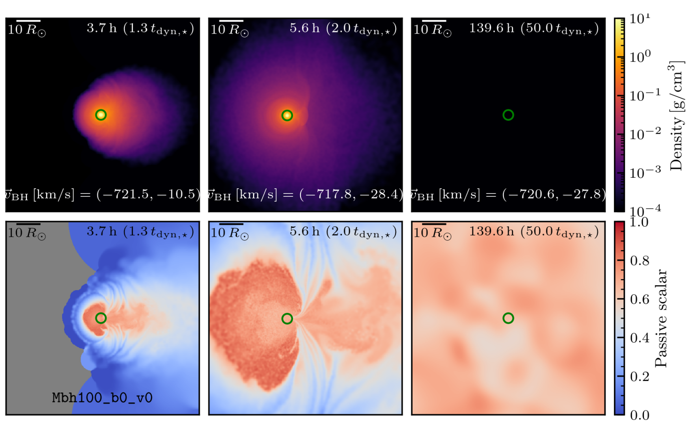

(e) BH mass 100 $M_\odot$. Head-on ($b = 0$) collision with $v_\infty = 0$. Panels in the right column are centered at the sBH's location.

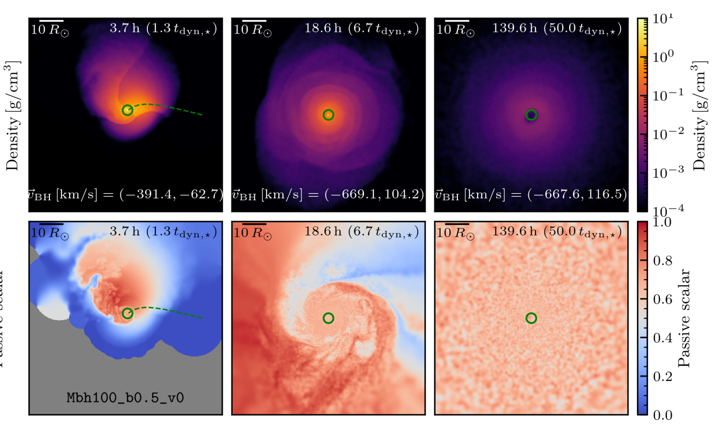

(f) BH mass 100 $M_\odot$. Grazing ($b = 0.5\,R_\star$) collision with $v_\infty = 0$. Panels in the right two columns are centered at the sBH's location.

Figure 4. Visualization of a subset of our simulations. In each sub-figure, we show the distribution of density (*top panels*) and passive scalar (*bottom panels*) at the mid-plane ($z = 0$), and the sBH's location (*green circle*), for snapshots at different evolutionary stages (as labeled in each panel). We default to the lab frame unless otherwise mentioned. We also label the velocity of the sBH in the lab frame. For grazing collisions ($b \neq 0$), we plot the trajectory of the sBH (*green dashed*).

dashed lines for its trajectory). As in the head-on case, the BH velocity is reversed by $t = 12\,\mathrm{h}$, and the BH is fully damped by the end of the simulation.

When the initial velocity is sufficiently high, however, the BH can penetrate and escape the star, with a post-encounter speed exceeding the local escape velocity. Figure 4c and 4d illustrate this regime: for both head-on and grazing geometries, the BH escapes when $v_\infty = 2v_0 \approx 2302\,\mathrm{km\,s^{-1}}$. The stellar interior is strongly mixed along the shock wake, yet the star remains gravitationally bound and undergoes sustained radial oscillations in response to the passing BH's perturbation.

Figures 4e and 4f present the same suite of collisions for a $100\,M_\odot$ BH, equal to the stellar mass. Compared with the $10\,M_\odot$ case, the more massive BH experiences a stronger drag force (cf. Equation 1, where $F_{\mathrm{drag}} \propto M_\bullet^2$) and exerts a deeper gravitational potential well, attracting more ambient gas. The BH is not represented by a sink-cell, i.e. we do not take into account of its accretion and the associated radiative feedback. As an approximation, we modify BH's gravitational potential with an arbitrarily-specified softening length equals $0.5R_\odot$ such that BH's gravity would be suppressed in its close proximity. In the head-on cases, the BH accumulates a gas envelope even during the high-velocity collision at $v_\infty = 2v_0 \approx 3104\,\mathrm{km\,s^{-1}}$. However, this envelope is dynamically disrupted following the violent shock interaction, and in both cases it is stripped by the end of the simulation.

The grazing geometry produces qualitatively different behavior. At $v_\infty = 0$ and $b = 0.5\,R_\star$ (Figure 4f), the angular momentum of the encounter causes the star to deform and spiral around the $100\,M_\odot$ BH, ultimately forming a rotationally supported, disc-like envelope by $t = 19\,\mathrm{h}$. The buildup of high temperature and pressure gradient in the disc around the BH's softened potential marginally suppresses gravitational instability and the excitation of global spiral structure. Although the disc loses mass continuously and is susceptible to marginal dynamical instabilities, it survives until the end of the simulation. At high collisional velocity ($v_\infty = 2v_0 \approx 3104\,\mathrm{km\,s^{-1}}$; not shown here), the BH escapes before a disc can form, and the star is heavily disrupted.

3.2.2. *BH retention in the star*

Figure 5 quantifies whether the BH is efficiently damped by gas drag and retained within the star, using the relative velocity between the BH and the stellar center of mass throughout the evolution, $|\boldsymbol{v}_\bullet - \langle \boldsymbol{v}_{\mathrm{gas}} \rangle|$, where $\langle \boldsymbol{v}_{\mathrm{gas}} \rangle$ is the mass-weighted center-of-mass velocity of all gas cells (note that our simulations employ equal-mass cells). The relative velocity at $t = 0$ corresponds to the initial separation of $2\,R_\star$ and is distinct from v_∞.

For most simulations, the relative velocity is damped to $\sim 0\,\mathrm{km\,s^{-1}}$ within $\sim 100\,\mathrm{h}$; for the remainder it is not. This is broadly consistent with semi-analytic simulations (Figures 1, 2). Yet hydrodynamical simulations find more outcomes in terms of the gas morphology, which we classify into three cases.

1. *The BH is retained in a spherical, dense envelope.* The BH velocity is efficiently damped, and the BH settles at the stellar center surrounded by a dense ($\sim 1\,\mathrm{g\,cm^{-3}}$) envelope (cf. Figures 4a and 4b). As shown in Figure 5, this outcome is typical for low-velocity ($v_\infty/v_0 \lesssim 1$) collisions with low-mass ($M_\bullet \lesssim 10\,M_\odot$) BHs. More massive BHs can also acquire an envelope, but only in head-on, low-velocity ($v_\infty/v_0 \lesssim 1$) collisions.

2. *The BH is retained in a disc-like, rotating envelope.* The BH is massive enough to heavily deform the star, and the orbital angular momentum drives the formation of a disc-like envelope (cf. Figure 4f). This outcome occurs for low-velocity ($v_\infty/v_0 \lesssim 1$), grazing collisions with high-mass ($M_\bullet \gtrsim 100\,M_\odot$) BHs. This outcome may represent the micro-TDE studied in previous works (e.g., Kremer et al. 2022).

3. *The BH escapes without forming an envelope.* The BH impacts the star at sufficiently high velocity that gas drag is unable to halt it (cf. Figures 4c and 4d). This outcome occurs for high-velocity ($v_\infty/v_0 \gtrsim 2$) collisions. An exception arises for light BHs (e.g., $5\,M_\odot$), whose weaker drag force (cf. Equation 1) allows escape even at moderate velocity ($v_\infty/v_0 = 1$).

For cases in which the BH is retained within the stellar material, we examine the envelope mass and radius in Figure 6. The envelope mass is defined as the gas gravitationally bound to the BH+envelope system, i.e., satisfying $\Phi + \gamma e + |\boldsymbol{v} - \boldsymbol{v}_\bullet|^2/2 < 0$, where Φ is the gravitational potential and γe is the specific enthalpy; the half-mass radius is evaluated accordingly. A quasi-hydrostatic BH* is only achieved for $M_\bullet \lesssim 10\,M_\odot$, in which case the envelope retains most of the original stellar mass and the half-mass radius remains approximately steady (modulo radial oscillations). For more massive BHs ($M_\bullet \gtrsim 30\,M_\odot$), the envelope loses mass while expanding, reaching at most $\lesssim 50\,M_\odot$, and does not attain a quasi-hydrostatic state within the simulation time.

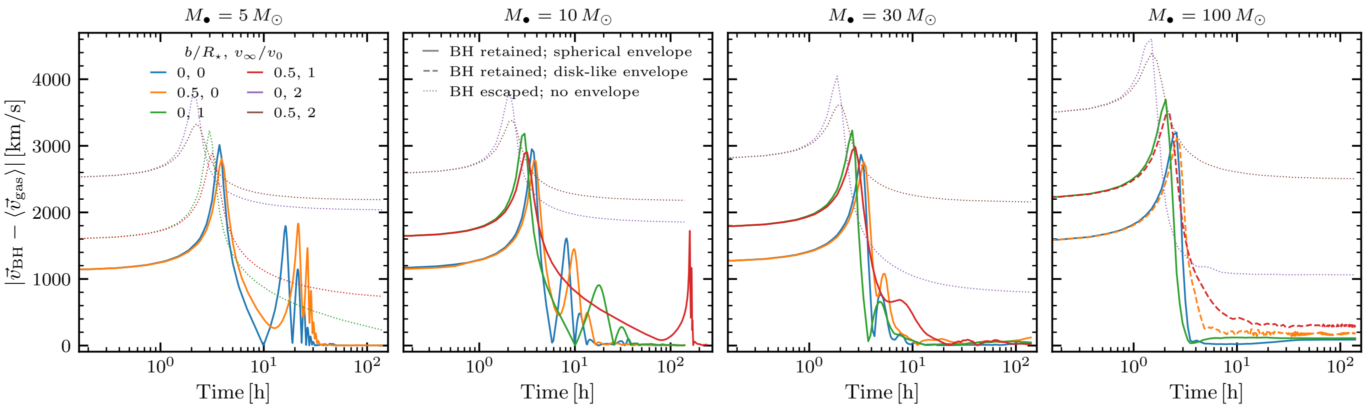

Figure 5. The relative velocity between the BH and star. This quantity is evaluated as $|\boldsymbol{v}_\bullet - \langle \boldsymbol{v}_{\rm gas} \rangle|$, where $\langle \boldsymbol{v}_{\rm gas} \rangle$ is the center-of-mass velocity for gas. Each panel represents the collisional simulations of different BH masses (as labeled above), where we plot the BH-gas relative velocity for collisions with varying b and v_∞. The possible outcome of each collision is classified as either a BH* with a spherical envelope (*solid*), a BH with a disk-like envelope (*dashed*), or a "bare" BH without an envelope (*dotted*).

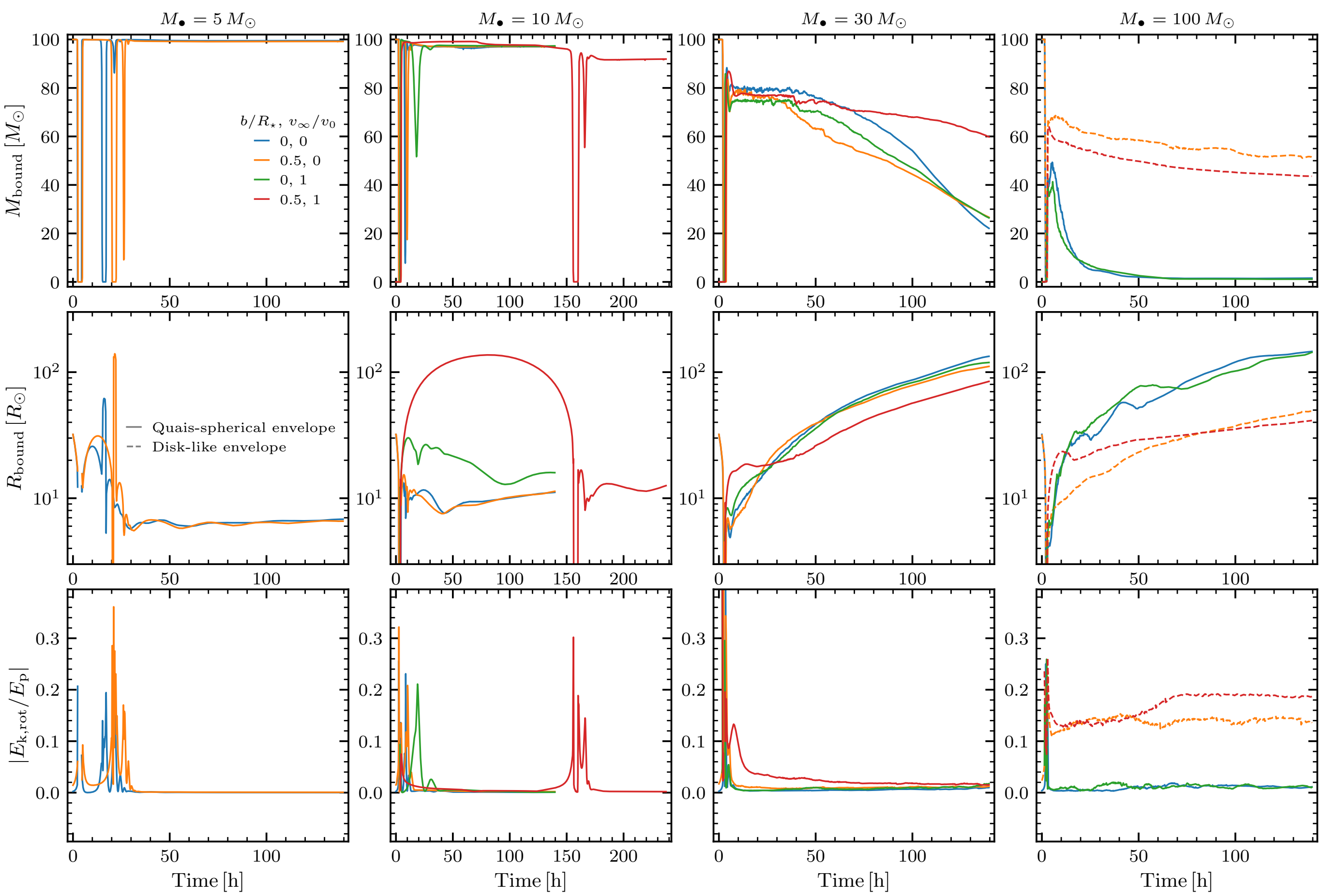

Figure 6. Envelope mass (*upper panels*), half-mass radius (*middle panels*), and $|E_{\rm k,rot}/E_{\rm p}|$ (*bottom panels*) of the BH* system for different collisional experiments. Here $|E_{\rm k,rot}/E_{\rm p}|$ represents the ratio between the rotational kinetic energy and the potential energy for the gaseous envelope. Each column corresponds to the labeled BH mass. Solid and dashed lines distinguish quasi-spherical and disc-like envelopes, respectively.

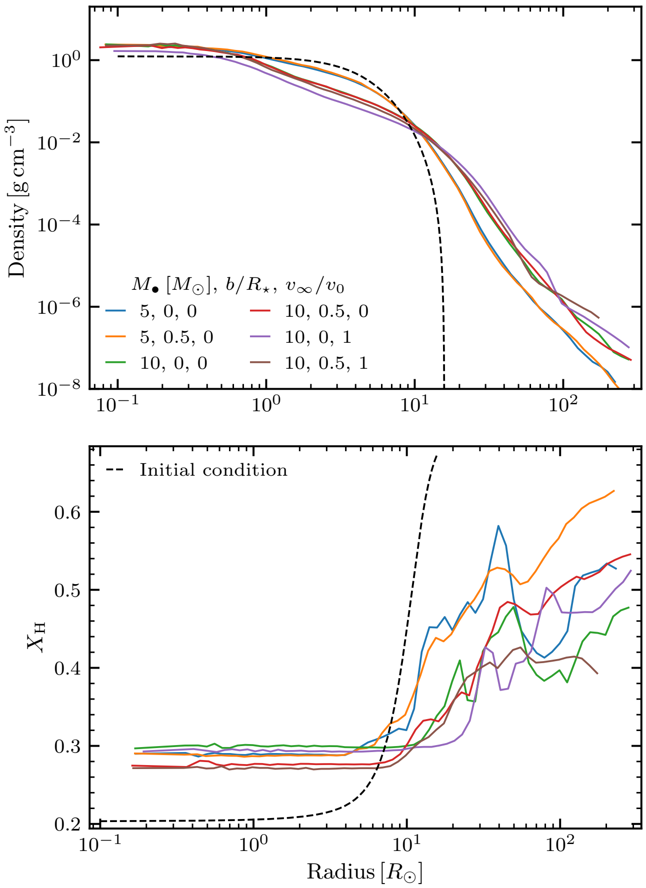

Figure 7. Radial density (*upper panel*) and mock hydrogen abundance ($X_{\rm H}$; *lower panel*) profiles of the BH*s produced in this work. Black dashed lines show the initial conditions. The $X_{\rm H}$ profile is a mock pre-collision distribution, post-processed to obtain the final abundance after mixing.

In the bottom panels of Fig. 6, we show the time evolution of the ratio $|E_{\rm k,rot}/E_{\rm p}|$ (ratio between the rotational kinetic energy and the potential energy), as an indicator of whether the envelope is rotationally dominated. Both quantities are derived from gas particles in the simulations, where $E_{\rm k,rot} = \sum_i m_i v_{{\rm rot},i}^2$, where $v_{{\rm rot},i}$ is the rotational (tangential) velocity in the xy plane for each gas particle, which is defined as $v_{{\rm rot},i} = j_{z,i}/r_{\rm 2D} = (xv_y - yv_x)_i/\sqrt{x_i^2+y_i^2}$. The potential energy is $E_{\rm p} = \sum_i m_i \Phi_i$. For most collisions, $|E_{\rm k,rot}/E_{\rm p}| \sim 0$ at the end of the simulations; however, for $M_\bullet = 100\,M_\odot$ and $b > 0$, $|E_{\rm k,rot}/E_{\rm p}| \sim 0.1$–$0.2$. This quantifies that a rotation-supported, disk-like envelope forms for massive sBHs with $M_\bullet = 100\,M_\odot$.

3.2.3. *BH* radial structure*

Of all collisional simulations, only 6 produce quasi-hydrostatic BH*s; these are examined further here. Figure 7 shows their radial density profiles. Relative to the initial main-sequence star (modeled as a $100\,M_\odot$, $n = 2.75$ polytrope), the gas envelope of the BH* is substantially more extended following the collision, while the central gas density in the vicinity of the BH remains $\sim 1\,{\rm g\,cm^{-3}}$, comparable to the pre-collision value.

We also quantify the redistribution of chemical elements by adopting a mock pre-collision hydrogen abundance profile motivated by nuclear burning: $X_{\rm H} = 0.2 + 0.5/[1+\exp(-(r-r_{\rm c})/2)]$, where $r_{\rm c} = 8\,R_\odot$. Post-processing the simulations by advecting the cells yields the final radial $X_{\rm H}$ distribution. Compared with the initial profile, the central hydrogen abundance is elevated to ~ 0.3 from 0.2. However, whether this hydrogen replenishment will extend the nuclear-burning time remains uncertain, since the BH* may be partially powered by the central accreting BH rather than entirely by nuclear reactions (Begelman et al. 2008).

4. ASTROPHYSICAL IMPLICATIONS

In this section, we discuss the astrophysical implications of these BH*s that arise from star–sBH collisions.

4.1. *Sequential evolution of the BH**

While our simulations generate hydrostatic structures, the long-term evolution of these BH*s remains uncertain. Below are some speculations.

When the embedded BH is much less massive than its host star, its accretion luminosity can be only a small fraction of the stellar nuclear luminosity, so the global stellar structure is expected to remain largely unchanged. For retained BHs whose mass becomes $\lesssim 10\%$ of the remaining stellar mass, the accretion luminosity, $L_{\rm acc} \sim \eta \dot{M}_\bullet c^2$, may exceed that generated by nuclear burning (Begelman et al. 2008; Ball et al. 2011; Coughlin & Begelman 2024). Since the stellar core is extremely optically thick, the energy flux from the BH is capped by convection, at $F_{\rm conv} \sim pc_{\rm s}$. The exact luminosity is mass-dependent (Coughlin & Begelman 2024): a massive central BH may generate a luminosity that is super-Eddington for the stellar mass, making the BH* thermally unstable and explode like a transient; while a BH* with a low-mass BH may remain thermally stable, until BH growth breaks up the stability (Hassan et al. 2026). This uncertainty should be ultimately addressed with stellar evolution modeling.

A detailed calculation of the spectral energy distribution of BH*s remains beyond the scope of this work. However, similar objects have recently been proposed to explain LRDs (e.g., Begelman & Dexter 2026; Inayoshi et al. 2026), although the BH*s studied here are considerably less massive.

4.2. *Gravitational-wave events*

Dense star clusters and AGN disks are the two leading formation channels for stellar-mass BH mergers, and both environments naturally contain main-sequence stars. Previous studies have shown that star–sBH collisions occur in both settings (Tagawa et al. 2020; Chen & Lin 2024; Rantala et al. 2024), raising the possibility that a BH binary may merge *inside* a stellar envelope.

A possible evolutionary pathway is that a stellar-mass BH is first captured by a massive star, forming a BH*. A second BH subsequently collides with the BH*, loses orbital energy through gas drag, and forms a bound binary with the embedded BH. Gas drag and gravitational torques may then accelerate the inspiral toward merger.

As an illustration, two $10\,M_\odot$ BHs in a circular orbit with semi-major axis $a = 0.1\,R_\odot$ would merge through gravitational-wave emission alone in

$$\tau_{\rm merge} = \frac{5}{256}\frac{c^5 a^4}{G^3 m_1 m_2 (m_1 + m_2)} \approx 7.5\,{\rm yr}, \qquad (9)$$

with eccentric binaries merging considerably faster (Peters 1964). Gas drag is expected to shorten this timescale further (O'Neill et al. 2024).

A BH merger in the stellar envelope could also produce an electromagnetic counterpart: energy deposited into the envelope by the GW recoil, or post-merger accretion onto the remnant BH, may generate optical or X-ray emission.

4.3. *Dense star clusters*

In dense stellar clusters, repeated star–BH collisions may provide a new pathway for IMBH formation. The standard picture invokes runaway stellar collisions that assemble a supermassive star (SMS), which subsequently collapses into an IMBH (e.g., Portegies Zwart & McMillan 2002; Kremer et al. 2020; Shi et al. 2021; Rantala et al. 2024). Hierarchical BH mergers offer an alternative route but are generally limited by the long timescales required to harden BH binaries (e.g., Kritos & Silk 2026).

Our simulations suggest a different evolutionary pathway. Stellar-mass BHs can be captured and retained by an SMS, forming a BH*. Repeated star–BH collisions then deliver additional BHs to the stellar center, where sequential BH mergers gradually build up the central BH while the stellar envelope remains intact. Whether the merger product is retained depends on the competition between GW recoil kicks and the escape velocity of the SMS. For $M_{\rm SMS} \sim 10^3$–$10^4\,M_\odot$ and $R_{\rm SMS} \sim 10^3\,R_\odot$, the escape velocity is $v_{\rm esc} \sim$ few $\times\, 10^2\,{\rm km\,s^{-1}}$, comparable to typical GW recoil velocities (e.g., Holley-Bockelmann et al. 2008). Recoils are suppressed for unequal-mass mergers or favorable spin configurations, while gas drag within the stellar envelope may further enhance BH retention. This scenario naturally bridges the formation of an SMS and the subsequent growth of an IMBH.

This mechanism may also be relevant to the luminous red dots (LRDs) discovered by JWST at $z \gtrsim 4$ (e.g., Matthee et al. 2024), for which BH* models have recently been proposed (de Graaff et al. 2025a; Begelman & Dexter 2026; Sun et al. 2026; Inayoshi et al. 2026). Once the first BH* forms through a star–BH collision, subsequent runaway stellar collisions can replenish the envelope, while additional stellar-mass BHs are efficiently captured and merge with the central BH (also see Rantala 2026). Quantifying the importance of this channel requires realistic models of collision rates and BH growth, which we leave for future work.

4.4. *AGN disks*

AGN disks provide another promising environment for BH* formation because frequent star–BH encounters are expected in their dense gaseous disks (e.g., Chen & Lin 2024), while the high ambient gas density fundamentally modifies stellar evolution (e.g., Cantiello et al. 2021; Ali-Dib & Lin 2023; Xu et al. 2026). Star–sBH collisions may produce BH*s in these environments, and they may also reach an accretion–wind equilibrium in the disk, potentially leading to a distinct class of stellar evolution.

Moreover, high-velocity encounters can strongly perturb the star. Shock heating mixes the stellar interior and ejects part of the envelope into the surrounding AGN disk, contributing to the chemical enrichment. Such enrichment may help explain the anomalous abundance patterns inferred from AGN broad-line regions (e.g., Isobe et al. 2025) if the star–sBH collision rates are sufficiently high (e.g., $10^{-6}\,{\rm yr}^{-1}$ per star).

5. CONCLUSIONS

In this work, we have studied collisions between stellar-mass black holes (sBHs) and a $100\,M_\odot$ main-sequence star using both semi-analytic and hydrodynamical simulations. While the outcomes of star–sBH collisions depend on $M_\bullet/M_\star$ and other velocity parameters, we focused on the case of $M_\bullet/M_\star \lesssim 1$ and *direct geometric collision*. Our main findings are as follows.

1. *BHs with $M_\bullet \lesssim 0.2\,M_\star$ can be retained after low-velocity collisions with stars to form a BH*,* as predicted from both our semi-analytic and hydrodynamical simulations. These collision produces a *quasi-hydrostatic BH** with a dense ($\sim 1\,{\rm g\,cm^{-3}}$), spherical, and extended envelope that retains most of the original stellar mass. Our one-dimensional heating calculations indicate that no thermal runaway will be triggered during this process.

2. *BHs with $M_\bullet \gtrsim 0.2\,M_\star$ may not form a BH* with substantial retained envelopes through sBH–star collisions.* Above this critical mass, the shock heating released by gas drag is capable to disrupt the star. The envelope is quasi-spherical in head-on collisions and disc-like in grazing ones; however, in both cases the envelope is dynamically unstable, resulting substantial mass loss and a transient event like a micro-TDE (e.g., Perets et al. 2016; Kremer et al. 2022).

3. *BH retention depends on impact velocity.* Gas drag efficiently retains the BH within the stellar envelope for impact velocities $v_\infty \lesssim 2v_0 = 2\sqrt{G(M_\star + M_\bullet)/R_\star}$. Above this threshold, the BH penetrates and escapes the star. Light BHs ($M_\bullet \lesssim 5\,M_\odot$) experience weaker drag and may escape even at $v_\infty \sim v_0$. Otherwise, the BH retention happens quickly, usually within several hundreds of hours (several tens of $\tau_{\mathrm{dyn},\star}$).

4. *The collision drives large-scale chemical mixing.* The shock wake of the BH advects hydrogen-rich material from the envelope into the core, elevating the central hydrogen abundance from its pre-collision value (e.g., X_H rises from 0.2 to ~ 0.3 in our mock test). This replenishment of core hydrogen may impact on the long-term evolution of the BH*. Compared with the progenitor star, the BH* envelope is substantially inflated after formation, while the central density near the BH remains comparable to that of the original star.

These results have several astrophysical implications. First, sBH binaries formed inside a BH* can merge via GW emission on timescales of $\sim$ years, producing a signal that is distinct from a vacuum BH–BH merger due to the friction from the surrounding gas or an electromagnetic counterpart. Second, in dense star clusters, repeated star–sBH collisions can migrate multiple sBHs to the center of a supermassive star, driving sequential mergers that rapidly build an increasingly massive central BH. Whether the merger product is retained depends on the competition between GW recoil kicks and the confining gas drag of the stellar envelope. This channel offers a formation pathway for IMBHs and may be relevant to the massive BHs inferred in the LRDs observed at $z \gtrsim 4$ by JWST. Third, in AGN disks, star–sBH collisions alter stellar evolution by replenishing core hydrogen and, in violent encounters, ejecting nucleosynthesis-enriched material into the disk, contributing to chemical enrichment distinct from supernovae or stellar winds.

BH*s in this work are not essentially stable in the long term, since our simulations track only the BH* formation that completes on the stellar dynamical timescale. The subsequent thermal relaxation and long-term evolution, including BH accretion, radiative feedback, and the eventual fate of the BH*, require dedicated stellar evolution modeling (at least for the typical parameter space explored here; Hassan et al. 2026). In a companion paper, we study the formation of sBH binaries inside BH*s in detail. Future work should also address aspects like the observational signatures of such BH*s.

We thank Sizheng Ma and Hongxuan Jiang for sharing the results of their simulations and close interaction. We also benefited from useful conversations with Long Wang and Yixian Chen. YS and NM acknowledge the support of the Natural Sciences and Engineering Research Council of Canada (NSERC) under funding reference No. 568580. QH acknowledges the support of the National Natural Science Foundation of China (grant No. 12173021 and 12133005). Computations were performed on the "Trillium" supercomputer at the SciNet HPC Consortium. SciNet is funded by Innovation, Science and Economic Development Canada; the Digital Research Alliance of Canada; the Ontario Research Fund: Research Excellence; and the University of Toronto.

Software: `REBOUNDx` (Tamayo et al. 2020); `MESA` (Paxton et al. 2011, 2013, 2015, 2018, 2019; Jermyn et al. 2023); `GIZMO` (Hopkins 2015)

REFERENCES

Ali-Dib, M., & Lin, D. N. C. 2023, MNRAS, 526, 5824, doi: 10.1093/mnras/stad2774

Ball, W. H., Tout, C. A., Żytkow, A. N., & Eldridge, J. J. 2011, MNRAS, 414, 2751, doi: 10.1111/j.1365-2966.2011.18591.x

Begelman, M. C., & Dexter, J. 2026, ApJ, 996, 48, doi: 10.3847/1538-4357/ae274a

Begelman, M. C., Rossi, E. M., & Armitage, P. J. 2008, MNRAS, 387, 1649, doi: 10.1111/j.1365-2966.2008.13344.x

Binney, J., & Tremaine, S. 2008, Galactic Dynamics: Second Edition

Bondi, H. 1952, MNRAS, 112, 195, doi: 10.1093/mnras/112.2.195

Cantiello, M., Jermyn, A. S., & Lin, D. N. C. 2021, ApJ, 910, 94, doi: 10.3847/1538-4357/abdf4f

Chandrasekhar, S. 1943, ApJ, 97, 255, doi: 10.1086/144517

—. 1957, An introduction to the study of stellar structure.

Chen, Y.-X., & Lin, D. N. C. 2024, ApJ, 967, 88, doi: 10.3847/1538-4357/ad3c3a

Coughlin, E. R., & Begelman, M. C. 2024, ApJ, 970, 158, doi: 10.3847/1538-4357/ad5723

Cruz-Osorio, A., & Rezzolla, L. 2020, ApJ, 894, 147, doi: 10.3847/1538-4357/ab89aa

de Graaff, A., Hviding, R. E., Naidu, R. P., et al. 2025a, arXiv e-prints, arXiv:2511.21820, doi: 10.48550/arXiv.2511.21820

de Graaff, A., Rix, H.-W., Naidu, R. P., et al. 2025b, A&A, 701, A168, doi: 10.1051/0004-6361/202554681

Edgar, R. 2004, NewAR, 48, 843, doi: 10.1016/j.newar.2004.06.001

Generozov, A., & Perets, H. B. 2023, MNRAS, 522, 1763, doi: 10.1093/mnras/stad1016

Hassan, J. B., Perna, R., Cantiello, M., et al. 2026, ApJ, 998, 65, doi: 10.3847/1538-4357/ae3002

Hirai, R., & Podsiadlowski, P. 2022, MNRAS, 517, 4544, doi: 10.1093/mnras/stac3007

Holley-Bockelmann, K., Gültekin, K., Shoemaker, D., & Yunes, N. 2008, ApJ, 686, 829, doi: 10.1086/591218

Hopkins, P. F. 2015, MNRAS, 450, 53, doi: 10.1093/mnras/stv195

Hopkins, P. F., Nadler, E. O., Grudić, M. Y., et al. 2023, MNRAS, 525, 5951, doi: 10.1093/mnras/stad2548

Hoyle, F., & Lyttleton, R. A. 1939, Proceedings of the Cambridge Philosophical Society, 35, 405, doi: 10.1017/S0305004100021150

Inayoshi, K., & Ho, L. C. 2025, arXiv e-prints, arXiv:2512.03130, doi: 10.48550/arXiv.2512.03130

Inayoshi, K., & Maiolino, R. 2025, ApJL, 980, L27, doi: 10.3847/2041-8213/adaebd

Inayoshi, K., Murase, K., & Kashiyama, K. 2026, ApJ, 1000, 90, doi: 10.3847/1538-4357/ae42ce

Isobe, Y., Maiolino, R., D'Eugenio, F., et al. 2025, MNRAS, 541, L71, doi: 10.1093/mnrasl/slaf056

Ivanova, N., Justham, S., Chen, X., et al. 2013, A&A Rv, 21, 59, doi: 10.1007/s00159-013-0059-2

Jermyn, A. S., Bauer, E. B., Schwab, J., et al. 2023, ApJS, 265, 15, doi: 10.3847/1538-4365/acae8d

Kıroğlu, F., Kremer, K., Biscoveanu, S., González Prieto, E., & Rasio, F. A. 2025, ApJ, 979, 237, doi: 10.3847/1538-4357/ada26b

Kocevski, D. D., Finkelstein, S. L., Barro, G., et al. 2025, ApJ, 986, 126, doi: 10.3847/1538-4357/adbc7d

Kokorev, V., Caputi, K. I., Greene, J. E., et al. 2024, ApJ, 968, 38, doi: 10.3847/1538-4357/ad4265

Kokorev, V., Chisholm, J., Naidu, R. P., et al. 2026, ApJ, 1004, 153, doi: 10.3847/1538-4357/ae4ed7

Kremer, K., Lombardi, J. C., Lu, W., Piro, A. L., & Rasio, F. A. 2022, ApJ, 933, 203, doi: 10.3847/1538-4357/ac714f

Kremer, K., Lu, W., Rodriguez, C. L., Lachat, M., & Rasio, F. A. 2019, ApJ, 881, 75, doi: 10.3847/1538-4357/ab2e0c

Kremer, K., Spera, M., Becker, D., et al. 2020, ApJ, 903, 45, doi: 10.3847/1538-4357/abb945

Kritos, K., & Silk, J. 2026, ApJ, 1004, 226, doi: 10.3847/1538-4357/ae731c

Lescaudron, S., Dubois, Y., Beckmann, R. S., & Volonteri, M. 2023, A&A, 674, A217, doi: 10.1051/0004-6361/202243392

Levesque, E. M., Massey, P., Zytkow, A. N., & Morrell, N. 2014, MNRAS, 443, L94, doi: 10.1093/mnrasl/slu080

MacLeod, M., & Ramirez-Ruiz, E. 2015a, ApJ, 803, 41, doi: 10.1088/0004-637X/803/1/41

—. 2015b, ApJL, 798, L19, doi: 10.1088/2041-8205/798/1/L19

Matthee, J., Naidu, R. P., Brammer, G., et al. 2024, ApJ, 963, 129, doi: 10.3847/1538-4357/ad2345

Murguia-Berthier, A., MacLeod, M., Ramirez-Ruiz, E., Antoni, A., & Macias, P. 2017, ApJ, 845, 173, doi: 10.3847/1538-4357/aa8140

Naidu, R. P., Matthee, J., Katz, H., et al. 2025, arXiv e-prints, arXiv:2503.16596, doi: 10.48550/arXiv.2503.16596

Naidu, R. P., Matthee, J., de Graaff, A., et al. 2026, arXiv e-prints, arXiv:2606.30711, doi: 10.48550/arXiv.2606.30711

Ohlmann, S. T., Röpke, F. K., Pakmor, R., & Springel, V. 2017, A&A, 599, A5, doi: 10.1051/0004-6361/201629692

O'Neill, D., D'Orazio, D. J., Samsing, J., & Pessah, M. E. 2024, ApJ, 974, 216, doi: 10.3847/1538-4357/ad7250

Ostriker, E. C. 1999, ApJ, 513, 252, doi: 10.1086/306858

Paxton, B., Bildsten, L., Dotter, A., et al. 2011, ApJS, 192, 3, doi: 10.1088/0067-0049/192/1/3

Paxton, B., Cantiello, M., Arras, P., et al. 2013, ApJS, 208, 4, doi: 10.1088/0067-0049/208/1/4

Paxton, B., Marchant, P., Schwab, J., et al. 2015, ApJS, 220, 15, doi: 10.1088/0067-0049/220/1/15

Paxton, B., Schwab, J., Bauer, E. B., et al. 2018, ApJS, 234, 34, doi: 10.3847/1538-4365/aaa5a8

Paxton, B., Smolec, R., Schwab, J., et al. 2019, ApJS, 243, 10, doi: 10.3847/1538-4365/ab2241

Perets, H. B., Li, Z., Lombardi, Jr., J. C., & Milcarek, Jr., S. R. 2016, ApJ, 823, 113, doi: 10.3847/0004-637X/823/2/113

Peters, P. C. 1964, Physical Review, 136, 1224, doi: 10.1103/PhysRev.136.B1224

Portegies Zwart, S. F., & McMillan, S. L. W. 2002, ApJ, 576, 899, doi: 10.1086/341798

Rantala, A. 2026, arXiv e-prints, arXiv:2604.22924, doi: 10.48550/arXiv.2604.22924

Rantala, A., Naab, T., & Lahén, N. 2024, MNRAS, 531, 3770, doi: 10.1093/mnras/stae1413

Rastello, S., Iorio, G., Gieles, M., & Wang, L. 2026, A&A, 707, A217, doi: 10.1051/0004-6361/202556781

Rein, H., & Liu, S.-F. 2012, A&A, 537, A128, doi: 10.1051/0004-6361/201118085

Rein, H., & Spiegel, D. S. 2015, MNRAS, 446, 1424, doi: 10.1093/mnras/stu2164

Ricker, P. M., & Taam, R. E. 2012, ApJ, 746, 74, doi: 10.1088/0004-637X/746/1/74

Röpke, F. K., & De Marco, O. 2023, Living Reviews in Computational Astrophysics, 9, 2, doi: 10.1007/s41115-023-00017-x

Rose, S. C., Naoz, S., Sari, R., & Linial, I. 2022, ApJL, 929, L22, doi: 10.3847/2041-8213/ac6426

Ryu, T., Perna, R., & Wang, Y.-H. 2022, MNRAS, 516, 2204, doi: 10.1093/mnras/stac2316

Shi, Y., Grudić, M. Y., & Hopkins, P. F. 2021, MNRAS, 505, 2753, doi: 10.1093/mnras/stab1470

Shi, Y., Huang, X., Lin, D. N. C., & Murray, N. 2026, arXiv e-prints, arXiv:2608.00242, doi: 10.48550/arXiv.2608.00242

Sun, W. Q., Naidu, R. P., Matthee, J., et al. 2026, The Open Journal of Astrophysics, 9, 62505, doi: 10.33232/001c.162505

Suzuguchi, T., Sugimura, K., Hosokawa, T., & Matsumoto, T. 2024, ApJ, 966, 7, doi: 10.3847/1538-4357/ad34af

Tagawa, H., Haiman, Z., & Kocsis, B. 2020, ApJ, 898, 25, doi: 10.3847/1538-4357/ab9b8c

Tamayo, D., Rein, H., Shi, P., & Hernandez, D. M. 2020, MNRAS, 491, 2885, doi: 10.1093/mnras/stz2870

Thorne, K. S., & Zytkow, A. N. 1977, ApJ, 212, 832, doi: 10.1086/155109

Tout, C. A., Pols, O. R., Eggleton, P. P., & Han, Z. 1996, MNRAS, 281, 257, doi: 10.1093/mnras/281.1.257

Tsuna, D., & Lu, W. 2025, ApJ, 986, 84, doi: 10.3847/1538-4357/add158

Volonteri, M., & Begelman, M. C. 2010, MNRAS, 409, 1022, doi: 10.1111/j.1365-2966.2010.17359.x

Vynatheya, P., Ryu, T., Pakmor, R., de Mink, S. E., & Perets, H. B. 2024, A&A, 685, A45, doi: 10.1051/0004-6361/202348357

Xin, C., Haiman, Z., Perna, R., Wang, Y., & Ryu, T. 2024, ApJ, 961, 149, doi: 10.3847/1538-4357/ad11d3

Xu, Z.-H. 2025, Research in Astronomy and Astrophysics, 25, 115013, doi: 10.1088/1674-4527/adfeb9

Xu, Z.-H., Chen, Y.-X., & Lin, D. N. C. 2026, ApJ, 997, 206, doi: 10.3847/1538-4357/ae2271

Yang, Y., Bartos, I., Fragione, G., et al. 2022, ApJL, 933, L28, doi: 10.3847/2041-8213/ac7c0b